Chapter 6

Wave Propagation in a Two-dimensional Colloidal System

In the previous chapter, we analyzed wave propagation through dry, one-dimensional micro-granular chains in air. The generalization of the results to two-dimensional, micro-granular lattices is an interesting fundamental question. Earlier experimental investigations of wave propagation in macroscopic two-dimensional granular lattices have shown that lattice configuration plays a crucial role in determining the possible traveling wave that is supported by the granular system [85, 128]. For example, in contrast to the one-dimensional system, no genuine traveling wave excitations with constant velocity have been found to persist in a hexagonal configuration [148]. The new dimensionality not only introduces more interaction between particles and more possible direction for wave propagation, but it also changes the behavior of mechanical wave transport within the system.

However, the dynamics of two- or three-dimensional ordered granular systems are relatively poorly understood. While it is suggested that a squared lattice granular system should behave similarly to a one-dimensional granular chain when the solitary wave is propagating along the lattice vectors, direct generalization of solitary wave solution to two- or three-dimensional systems has not yet been derived. Early experimental efforts by Shukla et al. use photoelasticity techniques (including cubic and hexagonal packing) to image wave propagation in various two-dimensional granular crystals [47, 79-84]. These researchers' experiments show that within higher dimensional granular crystals, the force load path is influenced by the contact angle between lattice elements and wave propagation is altered by the vectors connecting the centers of mass of the neighboring particles. The new dimensionality not only introduces more interaction between particles, but also brings new degrees of freedom for designing and engineering the lattice to achieve desired wave propagating properties. Leonard et al. studied the wave propagation in two-dimensional square lattice of spherical particles [85] and showed that by inserting cylindered intruders into square lattices of spherical particles, alternating both the wave direction and energy flux is possible [86].

The testing of two-dimensional granular systems has also been shown to be sensitive to the presence of defects and imperfections in the lattice packing. Experimental results of different two-dimensional arrangements of particles all showed that variations due to inter-particle gaps, surface defects, particle size variations, and the flatness of the supporting structure all affect the repeatability of the measured dynamic response. As the scale of the particles is reduced, these effects are expected to become more dominant, particularly in a dry environment where the physical contact between particles is not altered by surrounding media.

To overcome these limitations, we explore wave propagation in two-dimensional micro-granular systems that are immersed in a fluid environment. For this we test colloidal systems that are composed of SiO2 particles in a water glycerol solution. In these systems, hexagonal lattices of SiO_2 particles with a radius of 3.69 μm can be constructed using self-assembling techniques. We investigate these colloidal systems' dynamics by delivering controlled kinetic energy that is several orders of magnitude higher than the background kinetic energy to specific particles within them. With higher kinetic energy, we are able to observe the inter-particle interaction at a much higher velocity and consequently much smaller inter-particle distance. This allows us to characterize the particle-particle interactions and their roles in particle wave propagation within the colloidal systems.

6.1. Modeling the two-dimensional colloidal systems

The colloidal system of SiO_2 particles studied in this chapter differs from the dry particle system in the previous chapter not only due to the much smaller particles size, but also because of the presence of the background fluid. In this system, hydro-dynamic interactions between particles are a dominating factor in the dynamic response of the colloidal system. In the inertia regime, other types of forces such as lubrication hydrodynamic forces [122, 149], elastic contact forces [150], and even elatohydrodyamic forces [151, 152] might become significant in addition to the elastic inter-particle interactions. In this section, we detail the model that we developed for the colloidal systems. In this model, the inter-particle interactions between neighboring particles include contact forces, electrostatic forces, Stokes' drag forces, and hydrodynamic forces.

For particle i interacting with another particle j, the total force on particle i is

$$\vec{f_i} = \overrightarrow{f_{\text{stoke,ij}}} + \overrightarrow{f_{\text{electrostatic,ij}}} + \overrightarrow{f_{\text{hydro,ij}}} + \overrightarrow{f_{\text{contact,ij}}}, \tag{6.1}$$

where $\overrightarrow{f_{\text{electrostatic,ij}}}$ is the electrostatic force due to the surface charges on the particles, $\overrightarrow{f_{\text{stoke,i}}}$ is the Stokes' drag on particle i moving in the fluid, $\overrightarrow{f_{\text{electrostatic,ij}}}$, $\overrightarrow{f_{\text{hydro,ij}}}$, and $\overrightarrow{f_{\text{contact,ij}}}$ are respectively the electrostatic, hydrodynamic, and contact interactions between the two particles.

The electrostatic force, $\overrightarrow{f_{\text{electrostatic,ij}}}$, is formulated [153] as

$$\overrightarrow{f_{\text{electrostatic,ij}}} = \frac{1}{4\pi\varepsilon}\left(\frac{Z}{1+\kappa R}\right)^2 \left(\kappa \frac{e^{-\kappa D_{ij}}}{|\overrightarrow{X_i}-\overrightarrow{X_j}|} + e^{-\kappa D_{ij}} \frac{1}{|\overrightarrow{X_i}-\overrightarrow{X_j}|^2}\right), \tag{6.2}$$

where ε is the permittivity of the background medium, κ is the screening coefficient of the electrostatic force, Z is the surface charges, R is the radius of the particles, and $D_{ij} \equiv R_i + R_j - |\overrightarrow{X_i} - \overrightarrow{X_j}|$ is the distance between the surfaces of the two particles that are located at $\overrightarrow{X_i}$ and $\overrightarrow{X_j}$. Following the derivation in [149], the hydrodynamic force caused by the existence of the background fluid contributes to the dynamics with a velocity-dependent force that resists the relative motion in the normal direction, as well as with a tangential force between the two particles (when tangential motion exists):

$$\overrightarrow{f_{hydro,ij}} = \begin{pmatrix} f_{(hydro)n} \\ f_{(hydro)t} \end{pmatrix} = \begin{pmatrix} -6\pi\mu R^2/D_{ij} & \frac{12}{5}\pi\mu R\sqrt{2R/D_{ij}} \\ 0 & -2\pi\mu R\sqrt{2R/D_{ij}} \end{pmatrix} \begin{pmatrix} v_{n,ij} \\ v_{t,ij} \end{pmatrix}, \tag{6.3}$$

where μ is the dynamic viscosity of the background fluid. In reality, because of the surface roughness of the particles, two particles approaching each other would have contact before D_{ij} reaches zero. We define this distance as the cutoff distance D_{cut}, and Eq. (28) only holds when $D_{ij} > D_{cut}$. Once the two particles are in contact ($D_{ij} < D_{cut}$), the tangential force becomes zero, $f_{(hydro)t} = 0$, and the normal force is modified to:

$$f_{(hydro)n} = -6\pi\mu R^2 \frac{v_{n,ij}}{D_{ij}} \left(1 - \frac{\delta_{ij}}{D_{ij}}\right). \tag{6.4}$$

Here, $\delta_{ij} \equiv R_i + R_j + D_{cut} - |\overrightarrow{X_i} - \overrightarrow{X_j}|$ is the real deformation of the particles with the cut-off distance, D_{cut}, included. Correspondingly, the contact force, $\overrightarrow{f_{\text{contact,ij}}}$, is a modified version of Eq. (1) with D_{cut} included [154]:

$$f_{ij}(x_i, x_j) = \frac{4}{3}\frac{E_i E_j}{E_i(1-\nu_j^2)+E_j(1-\nu_i^2)}\sqrt{\frac{2R_iR_j}{R_i+R_j}}\left(R_i + R_j + D_{cut} - |x_i - x_j|\right)_+^{\frac{3}{2}}. \quad (6.5)$$

In this model, D_{cut} is an artificial cut-off distance between the hydrodynamic and contact interactions, which we estimated based on the experimentally measured roughness of the particles' surface. The parameters used in the model are listed in Table 6.1. With this model, we can simulate the wave propagation behavior at different initial velocities through a two-dimensional hexagonal lattice of particles.

Material properties	Values
D_{cut} (nm)	24
κ (1/nm)	1/300
Z (G)	600
E (GPa)	73.1
υ	0.17

Table 6.1: The parameters for numerical simulation with Eq. (6.1).

6.2. Excitation of mechanical waves in colloidal systems

In experiments, we begin by testing the dynamic response of the hexagonal lattice to a controlled energy input. The experimental setup has been described in Chapter 2. At first we create a hexagonal lattice within the micro-fluidic cell using the self-assembling techniques. In order to excite the transparent SiO_2 particles, we deposit a metal layer of SiO_2 particles and mix it with the uncoated one at a ratio of 1 to 500. Using the laser ablation technique, we excite the particles around the coated particle and observe the displacement of the surrounding particles with our high-speed imaging system at a rate of 311111 frames per second.

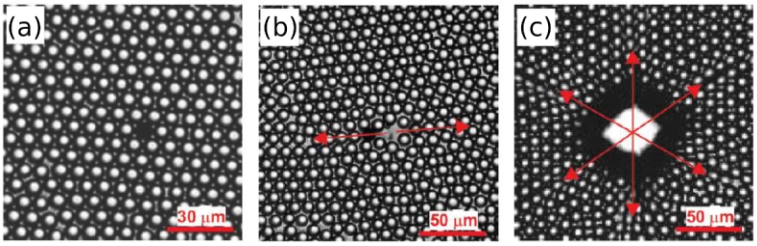

Figure 6.1: Images of laser excitation of micro-particles in a hexagonal lattice. (a) Photograph of a lattice prepared for laser excitation. The dark particle in the center is a micro-particle coated with 50 nm of Au that is targeted by the laser. (b) Excitation of the system with a weak laser pulse with energy of 0.1 μJ. The target particle obtains an initial

velocity in the direction of the red arrows. (c) Excitation of the system with a strong laser pulse of 0.25 μJ. Isotropic wave propagation in all directions is observed.

Fig. 6.1 shows the high-speed images of a typical response of the system to laser excitation. A coated particle originally at rest in a hexagonal lattice (Fig. 6.1a) is shot by weak (Fig. 6.1b) or strong (Fig. 6.1c) laser pulse. In the weak case, the laser energy projected onto the particle is 0.1 μJ and results in a linear motion of the excited particles along the red arrows. At higher power, a more isotropical displacement of particles occurs along the six preferred directions in the hexagonal lattice (which are labeled by the six red arrows in Fig. 6.1c). The difference between linear particle motion and isotropic excitation may be due to the initial disorder of the hexagonal lattice or the inhomogeneity of the coated surface.

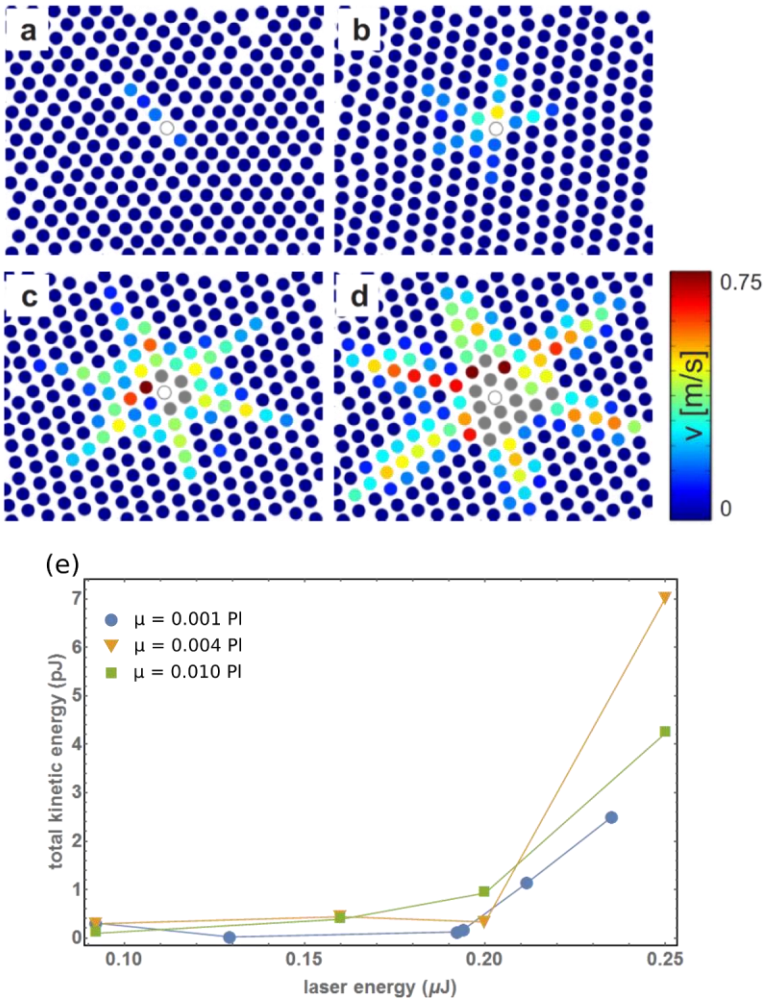

Figure 6.2: The velocity and kinetic energy transfers to the colloidal system by laser excitation. The velocity map of the system excited at (a) 0.13, (b) 0.19, (c) 0.21, and (d) 0.23 μJ shows that at lower energy (less than 0.15 μJ in our system), the laser can only excite the linear motion of the coated particles. At higher power the laser is capable of exciting mechanical impulses in all six hexagonal directions. The higher the laser energy, the farther the wave can reach out from the center. (e) The total kinetic energy of micro-particles in the lattice at different laser powers and background fluid viscosities. The energy transfer efficiency is about 0.001%, which is close to the efficiency when exciting one particle (see Chapter 3).

Using imaging processing techniques, we obtain the averaged velocities of the colloids in the lattice. An averaged velocity is defined as $\bar{v} \equiv \Delta x/\Delta t_c$, where Δx is the displacement observed in one frame and Δt_c is the sample interval of the high-speed camera (which is $1/311111$ in our system). We analyze the data of the colloidal system excited at different laser energy and plot the velocity map in Fig. 6.2. We can see decay of particle velocity over the distance from the center of laser impact. The

laser energy of the excitation is 0.13, 0.19, 0.21, and 0.23 μJ for Fig. 6.2a-d, respectively. At the low power excitation of 0.13 μJ, the linear excitation is observed again; while the laser energy increases, a more uniform displacement in all directions can be seen and the observed averaged velocity reaches out farther from the center of laser impact. While the exact mechanism of the laser excitation of the lattice is unclear given that the event happens much faster than the acquisition rate of our high-speed imaging system, the phenomenon is shown to be very reproducible and can be used as an experimental technique for exciting wave propagation in hexagonal lattices.

From the calibration of particle velocity at fixed laser energy and dynamic viscosity of the background fluid (Chapter 3), we know that the hydrodynamic properties of the background fluid are major factors influencing the laser excitation process. To gain more insight into the laser excitation, we vary the viscosity of the background fluid and calculate the total kinetic energy of all particles of the resulted measurement; the result is shown in Fig. 6.2e. Here we define the total kinetic energy of the system with the average velocity that we obtained from the experiment, $E_k = \sum m\bar{v}^2/2$, where m is the mass of the colloids. The efficiency of energy transfer is about 0.001%, which is very close to what we have seen in Chapter 3. Since the kinetic energy carried by the background fluid is not measurable using the imaging system, the results imply that the kinetic energies of the lattices excited by laser are mostly carried by the colloids that are visible experimentally. If this is true, our modeling of the colloids with particle-particle interaction (as opposed to a full hydrodynamic system that includes the fluid) should be sufficient for capturing most of the system's dynamics.

It is also interesting to see that the sample with viscosity equals to 0.004 Pl obtains more kinetic energy than the other two cases. When the laser excites the system, two competing factors influence the measured total energy: one is the higher efficiency of the PLA in fluid with higher viscosity, the other is the higher loss of kinetic energy due to higher viscosity. The first factor has already been discussed in Chapter 3; let us now consider the second one. If the colloids have a viscosity of μ, the Stokes' drag force ($f = -6\pi\mu Rv$) has a time constant of $2R^2\rho/9\mu$, which is 5.6, 1.4, and 0.56 μs for our SiO_2 particles when μ equals 0.001, 0.004 and 0.01, respectively. Considering our acquisition time of 3.3 μs, we expect very strong deceleration of the particles in the system with $\mu = 0.01\ Pl$, which explains the suppressed total kinetic energy. In the following work, we consider the laser excitation as a means to excite the six centermost particles simultaneously to the six hexagonal directions, with a controlled velocity that is determined by the laser energy and viscosity. Based on

this observation, we simulate wave propagation excited by laser in our colloidal system in the next section.

6.3. Mechanical wave propagation in colloidal systems

Until now we have been discussing the displacement and averaged velocities that are obtained experimentally. In order to gain more insight into the roles of different interactions between the particles in the system, in this section we perform numerical simulation of wave propagation. We start with the simulation of wave propagation behavior along the six branches of colloids in the hexagonal direction from the center (Fig. 6.3). In Fig. 6.3a, the coated particle is illustrated as the black particle in the center. After the laser excitation, the six neighboring particles obtain initial velocities and produce propagating waves in each hexagonal direction. We simulate the two-dimensional wave propagation with an initial velocity, v_{ini}, of 13 m/s, a viscosity of 0.004 Pl, and an initial distance between neighboring particles of 250nm. We choose a branch of particles from the six hexagonal directions and label those particles from 1 to 7. We plot the velocity of each particle in Fig. 6.3b and the inter-particle distance in Fig. 6.3d.

In Fig. 6.3d, we first notice that most of the evolution of the particles' velocities occurs within the first 200 ns and is quickly stabilized after 1 μs from the initial excitation. Since this is shorter than the minimal exposure time of our high-speed imaging system (2.7 μs), the details of the collision will not be resolved in the high-speed images; the measured displacement of the particle is the time-integration of velocity during the camera's acquisition time. In the first 200 ns, the particles collide with each other and pass on velocities along the chain. During this process, the velocities decay much faster than they do during the later period. The differences in velocity between particles are also being eliminated, and after the particles obtain similar velocities, their velocities decay exponentially. The fast elimination of velocity difference is the effect of the hydrodynamic force, $\overrightarrow{f_{hydro,ij}} \sim -\frac{6\pi\mu R^2}{D_{ij}} v_{ij} = -6\pi\mu \mathrm{R} \frac{R}{D_{ij}} v_{ij}$, which causes the relative velocities between neighboring particles, v_{ij}, to decrease. Notice that the hydrodynamic force differs with the Stokes' drag by a factor of $\frac{R}{D_{ij}}$. This is because in a close-packed lattice, $D_{ij} \ll R$, the hydrodynamic force is the dominant interaction that contributes to the decay of velocities before the velocity difference is eliminated. A closer look at the velocity of the first particle reveals a short period of acceleration after it collides with the second particle, which is again due to the hydrodynamic force resisting the separation of two particles.

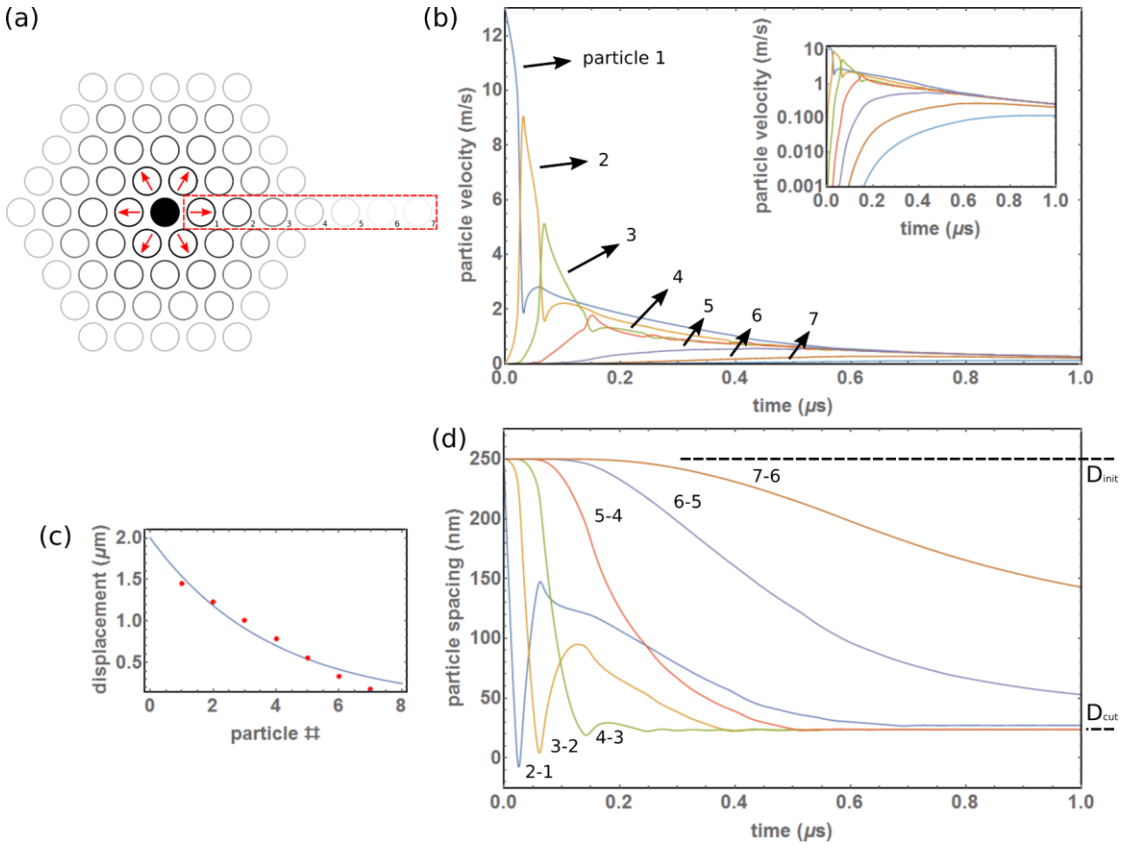

Figure 6.3: Numerical study of wave propagation along a chain within the hexagonal lattice. (a) Schematic diagram of the excitation and geometry of the lattice (b) The velocities of particles along the chain. (c) The total displacement (red dots) after the excitation obtained through simulation. It is fitted with an exponential decay formula and gives the decay length of 2.7. (d) The inter-particle distance during wave propagation.

In Fig. 6.3b, we also plot the same velocity result in log scale. It becomes clear that the final velocities of the particles approach the same value and results in the broadening of mechanical pulse. Due to the presence of the factor of $\frac{R}{D_{ij}}$ in hydrodynamic force, the broadening effects of hydrodynamic force on the traveling wave are more significant in a system where two particles can approach each other more closely. In our system this means when we have a higher initial velocity on the six centermost particles, the measured distance along the chain should decrease less since the particles obtain the same velocities more quickly than they do in the case of lower initial velocities.

It is noticeable that the velocity behavior of the first four particles is different from the behavior of later particles along the chain. The distinct behavior is due to the first four particles having reached

the regime of particle deformation. This deformation can be confirmed from Fig. 6.3d, in which the inter-particle distances between the first five particles have reach the cut-off distance, along with a faster bounce back. During the contact time, the particles transfer velocities via contact force, which is much more efficient than via hydrodynamic force. Whether a particle can reach the deformation regime is determined by whether its initial velocity is large enough to bring two particles into contact. In this case, the velocity barrier seems to be approximately 1 m/s.

To compare the simulation results with the experimental data of displacement, in Fig. 6.3c we plot each particle's final displacement, which decreases along the chain. To obtain a quantitative description of the decay, we fit the results with an exponential law of decay and obtain a decay constant of 28.2 μm.

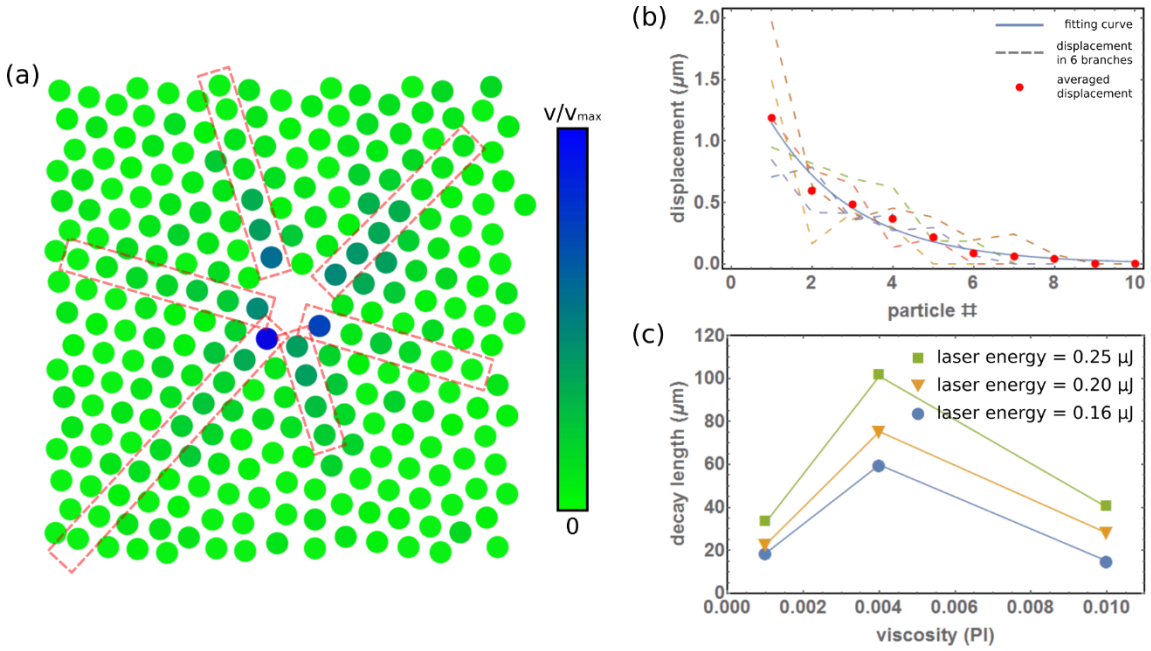

Figure 6.4: Experimental data of a wave propagation in the colloidal system with a viscosity of 0.01 Pl is excited by pulse energy of 0.16 μJ. (a) The measured velocity map of the system. The red boxes show the geometry of chains in the six hexagonal directions from the center particle. (b) The displacement of the particles that are shown in the red boxes in (a). (c) The decay length measured at different combinations of laser energy and viscosity.

In Fig. 6.4, we show experimental results of a velocity map of a system with a viscosity of 0.01 Pl as excited by pulse energy of 0.16 μJ. The six directions, which are marked by red boxes along the

lattice, and the displacement of particles within these boxes are shown by the dashed line in Fig. 6.2b. The decay can be seen from this dashed line. The averaged values (red dots) of the displacement at each distance are used to fit the exponential decay of the displacement along the chain. We obtain a decay length at varying laser energy and viscosity, as shown in Fig. 6.4c. The results show that for the same viscosity, the higher the laser energy (and initial velocities) are, the longer the decay length of the wave propagation. This agrees with the simulation, which indicates that a system with higher initial velocities will reach steady states (i.e., particles moving at the same velocities) faster and that the differences between the measured displacements along the chain will be smaller. With regard to the decay length obtained at the same laser energy, we expect it to be shorter given that at lower viscosity, the initial velocity excited by lasers will be less than in the case of higher viscosity. On the other hand, another competing factor is at play, namely the higher dissipation (and shorter decay length) due to higher viscosity. As a result we observe a shorter decay length of the same laser power at both low viscosity 0.001 (due to lower initial velocity) and high viscosity 0.01 (due to the higher dissipation).

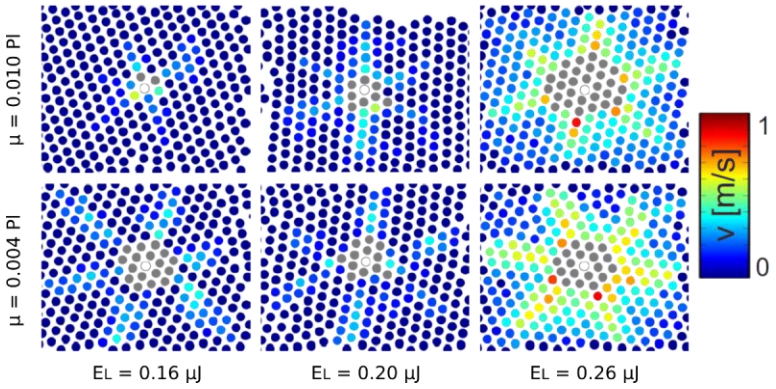

Figure 6.5: Velocity maps of the system tested at different laser energy and background fluid viscosity. The system is tested under a combination of viscosity equaling 0.001 Pl and 0.004 Pl and laser energy equaling 0.16, 0.20, and 0.25 μJ.

In Fig. 6.5, we show the experimental results of the velocity maps of systems of different viscosity as excited by different laser energy. Let us first compare images in the same column, which represents the system response at the same laser energy and different viscosity. The images with higher viscosity show shorter mechanical wave spans, which result from the high dissipation from higher viscosity. If we consider the fact that the laser transfers a higher initial velocity at higher viscosity, the effect of higher viscosity stopping the wave from reaching a farther distance from the center is even more

evident. Looking at the images in one row, we can see that at higher laser energy, the velocity distribution in the lattice becomes more isotropic. This can be explained by the tangential component of the hydrodynamic force, which is proportional to the tangential component of relative velocity between particles. Furthermore, at higher velocity, the particles in the chain in the six hexagonal directions could exert higher tangential force on the particles that are next to the chain. Since the hydrodynamic force is the main source for redistributing energy to the neighboring particles (other than the very small component of normal force that occurs when particles in the chain dislocate from their positions in an ideal lattice), a comparison of two systems dominated by the contact or hydrodynamic force will help to clarify the origin of isotropicity.

We simulate the behavior of two cases in which μ and v_{ini} are (a) 0.001 Pl, 8 m/s and (b) 0.004 Pl, 24 m/s. The higher initial velocity in the second case is included to account for the higher initial velocity that is obtained from the same laser energy acting on a system with higher viscosity. We obtain the evolution of the system at different time steps and plot the resultant velocity map in Fig. 6.6ab. In the fluid with a viscosity of 0.001 Pl, the wave propagates with little loss and redistribution to the other particles. In the fluid with a viscosity of 0.004 Pl, the wave decays faster and shows more isotropic propagation due to the strong hydrodynamic forces. The anisotropicity in the less viscous fluid comes from the fact that the deformation regime can easily be reached between the spheres in the branches due to lower hydrodynamic barriers. This allows more efficient momentum transfers between spheres in the branches, and as a result the hydrodynamic regime becomes less dominant in the evolution of the system and less energy is distributed onto the neighboring particles. These results indicate that the hydrodynamic force is the main contributing factor to the system's isotropicity.

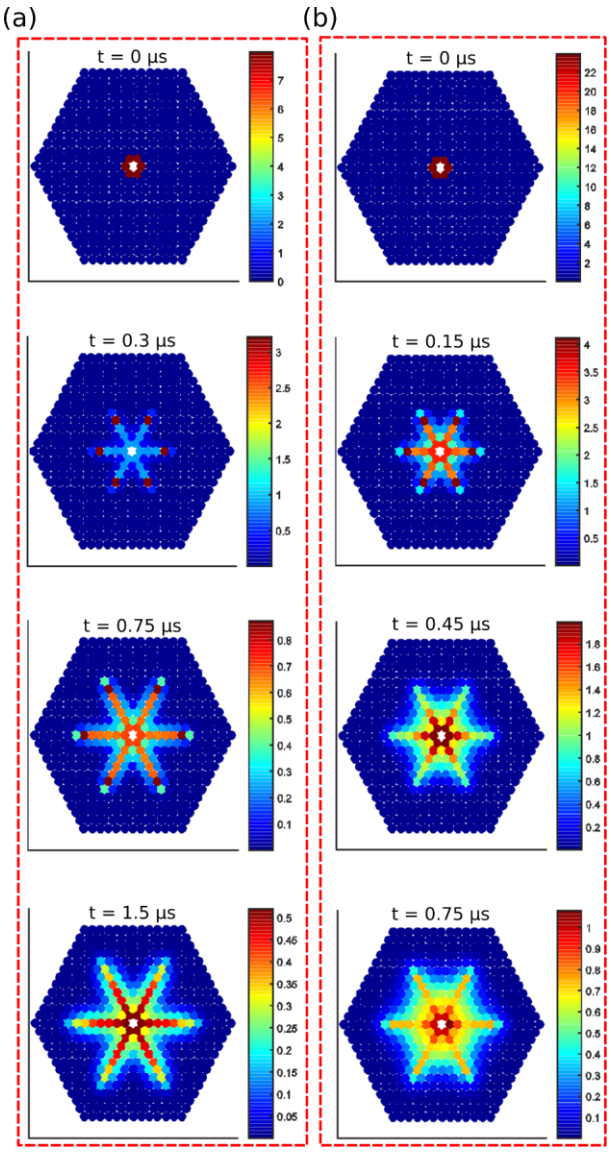

Figure 6.6 Numerical simulation of wave propagation generated with different initial velocities and fluid viscosities; μ and v_{ini} are (a) 0.001 Pl, 8 m/s and (b) 0.004 Pl, 24 m/s. The higher initial velocity in the second case is included to account for the higher initial velocity obtained from the same laser energy acting on a system with higher viscosity.

6.4. Summary

In this chapter we discussed the experimental and numerical examination of a two-dimensional micro-granular system that consists of a hexagonal lattice of SiO_2 particles with a radius of 3.69 μm. We performed the experimental examination by sending laser energy into the system to excite the initial velocity of one of the six centermost particles in the lattice. With the resultant velocity that is

high in comparison to traditional means, we are allowed to explore the system while the particles have enough velocity to break through the hydrodynamic barriers and to study wave propagation in systems of different viscosities. To capture the behavior of the system, we constructed a model that included the contact force, hydrodynamic force, electrostatic force, and Stokes' drag force and performed numerical simulation to study wave propagation at a time resolution higher than the one we used in our experimental system. The resultant simulation characterizes the roles of the hydrodynamic force and contact within wave propagation as well as explains the origins of isotropic wave propagation within the system.